applied optics

Plasmonic enhancement of photoacoustic-induced reflection changes

Guido de Haan,[1,2,†,*] Vanessa Verrina,[1,2,†] Aurèle J. L. Adam,[3] Hao Zhang,[1] and Paul C. M. Planken[1,2]

[1]Advanced Research Center for Nanolithography (ARCNL), Science Park 106, 1098 XG Amsterdam, The Netherlands
[2]Van der Waals-Zeeman Institute, University of Amsterdam, Science Park 904, 1098 XH Amsterdam, The Netherlands
[3]Optics Research Group, Department of Imaging Physics, Delft University of Technology, Lorentzweg 1, 2628 CJ Delft, The Netherlands
*Corresponding author: g.dehaan@arcnl.nl

Received 27 May 2021; revised 16 July 2021; accepted 20 July 2021; posted 22 July 2021 (Doc. ID 432659); published 16 August 2021

In this paper, we report on surface-plasmon-resonance enhancement of the time-dependent reflection changes caused by laser-induced acoustic waves. We measure an enhancement of the reflection changes induced by several acoustical modes, such as longitudinal, quasi-normal, and surface acoustic waves, by a factor of 10–20. We show that the reflection changes induced by the longitudinal and quasi-normal modes are enhanced in the wings of the surface plasmon polariton resonance. The surface acoustic wave-induced reflection changes are enhanced on the peak of this resonance. We attribute the enhanced reflection changes to the longitudinal wave and the quasi-normal mode to a shift in the surface plasmon polariton resonance via acoustically induced electron density changes and via grating geometry changes.

https://doi.org/10.1364/AO.432659

1. INTRODUCTION

Ultrafast optical pulses are capable of launching strain waves inside materials [1]. The fundamental understanding of the generation and propagation of these photo-induced acoustic echoes has grown dramatically in the past decades [2–6]. Furthermore, these photoacoustic waves have been used to study a variety of material properties and physical phenomena, such as thermal and electron diffusion [7–10], electron-hole plasmas in semiconductors [11], hot-electron-induced pressure [12,13], elastic constants of single layer [14–17] and multilayer structures [18,19], the electronic structure of materials [20,21], surface deformation dynamics [22–25], and the generation of terahertz radiation [26]. Furthermore, laser-induced acoustic echoes have been used for the detection of buried gratings [27,28], showing promise for applications in the semiconductor device manufacturing industry.

Generally speaking, laser-induced acoustic echoes can be detected by measuring changes in optical properties, such as reflection from and transmission through a material [4], or by diffracting light from an acoustic-wave-induced grating [23,27,29]. Changes in optical reflection caused by acoustic waves are usually small and thus require fairly complicated setups involving high-repetition-rate laser oscillators and signal modulation/demodulation techniques. Therefore, there is a clear need for a method to enhance the signal from acoustic waves, and one possible method to achieve this is to employ a plasmonic resonance.

Surface plasmon polaritons (SPPs) were first observed by Wood [30] in 1902 and have since been identified as collective electron oscillations coupled to an electromagnetic wave propagating along a metal–dielectric interface [31–33]. Surface plasmons can be generated in several different ways. The most common methods use the so-called "Kretschmann geometry" [34,35], and plasmonic gratings [36–38]. Plasmonic gratings have been used to create terahertz-frequency acoustic waves originating from a thin tellurium layer, formed by light-induced segregation in a (Cd, Mg)Te layer [39], and to study acoustic waves inside an acoustic cavity [40]. SPPs have also been used to detect and quantify strain waves in Au layers [41,42]. Furthermore, it has been shown that acoustic breathing modes in spherical nanoparticles, with diameters ranging from 15 to 120 nm, can change the localized plasmonic resonance of the particles [43–46]. Also, by using excitation and detection at a fixed wavelength, the angle-dependent plasmonic response to a longitudinal acoustic wave in a flat metallic layer in the Kretschmann geometry has been studied [13,35,47]. In general, however, surfaces are not flat. As a result, illumination of such a surface with a short laser pulse may give rise to the generation of additional kinds of acoustic waves, such as surface acoustic waves (SAWs) and even particle-like normal modes (NMs). The effect of these acoustic waves on the grating surface plasmon resonance is currently not well understood.

Here, we show an in-depth study of the effect of multiple types of acoustic waves on a plasmonic grating by measuring

the wavelength-dependent reflection changes in the vicinity of the SPP resonance. In our experiments, a 400 nm wavelength pump pulse illuminates the grating and a time-delayed probe-pulse tunable between 600 and 700 nm measures the changes in the reflection of the grating at wavelengths around the SPP resonance, located at 650 nm. Heating of the Au layer, including the grating, by the 400 nm pump leads to the generation of high-frequency acoustic waves in the material. Due to these high-frequency acoustic waves, we measure oscillatory changes of the reflection on the order of 1%. Analysis of these oscillations and their respective frequencies suggest that we observe multiple types of acoustic waves, three of which we identify as longitudinal waves (LWs) [3,27,28], surface waves [3,48–51], and grating line quasi-NM oscillations [50,52,53]. We find that the phase of the LWs and the grating line NMs experiences a π phase shift when the wavelength is tuned around the SPP resonance wavelength. Remarkably, we find that the optical response to the SAW is enhanced at the SPP resonance, whereas the longitudinal and grating line NMs are enhanced on the *slopes* of the resonance. The optical response of the Au may be attributed to two main effects: the acoustic-wave-induced material density changes, which in turn change the free-electron density, and the acoustic-wave-induced changes in the amplitude and duty cycle of the grating. Both of these effects give rise to a shift of the SPP resonance wavelength via a change in the plasma frequency and a change in the grating geometry, respectively. Both can explain the results for the longitudinal mode and the quasi-NM. The enhancement of the SAW on the peak of the SPP resonance is currently not understood. From the experiment, we estimate that the photoacoustic detection signals are enhanced 10–20-fold by measuring reflection changes on and around the SPP resonance.

2. EXPERIMENTAL SETUP

A schematic drawing of the experimental setup is shown in Fig. 1. An amplified Ti:Sapphire laser (Coherent Astrella) with a repetition rate of 1 kHz, a central wavelength of 800 nm, a pulse length of 35 fs, and a maximum pulse energy of 6 mJ is used for the experiments. The output of the laser is split into two beams using a 85/15 beam splitter.

The weaker beam passes through a variable optical delay line, after which the beam is frequency-doubled using a β-barium borate (BBO) crystal to generate 400 nm pulses. The beam passes through a mechanical chopper that is synchronized with the 1 kHz pulse train from the laser. With a 50% duty cycle, the chopper reduces the repetition rate of the pump to 500 Hz, so that every other pump pulse is blocked. After passing through dichroic mirrors, which filter out residual 800 nm light, the beam is focused onto the sample under an angle of incidence of approximately 5° to a spot size of approximately 400 μm. In this geometry, the pump pulses do *not* excite SPPs. In our experiments, these pump pulses have a pulse energy of about 12 μj.

The stronger 800 nm beam is sent to an optical parametric amplifier (OPA, HE-TOPAS, from Light Conversion). The OPA generates tunable infrared laser pulses with wavelengths ranging from 1200 to 1400 nm, with a maximum pulse energy

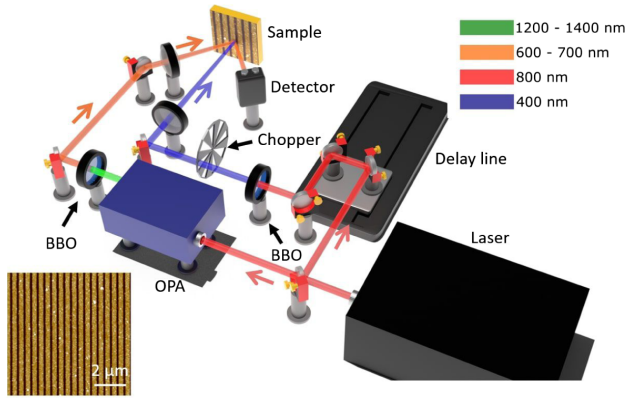

Fig. 1. Schematic drawing of the setup. The output from a 1 kHz repetition rate Ti:Sapphire amplified laser with a central wavelength of 800 nm is split into two parts. One beam (pump) is frequency-doubled to a wavelength of 400 nm by a BBO crystal and modulated by a mechanical chopper at 500 Hz. The other beam (probe) passes through a three-stage OPA, changing the wavelength to a tunable range from 1200 to 1400 nm. This beam is frequency-doubled by a BBO to a tunable wavelength range of 600–700 nm. Both the pump and the probe beam are focused onto the sample at angles of about 5° and 21°, respectively. The probe beam angle is chosen such that the SPP resonance is located at 650 nm. Projected on the sample, we show an AFM image of the Au grating, with a layer thickness of 177 nm, a pitch of 440 nm, and a duty cycle of 71%.

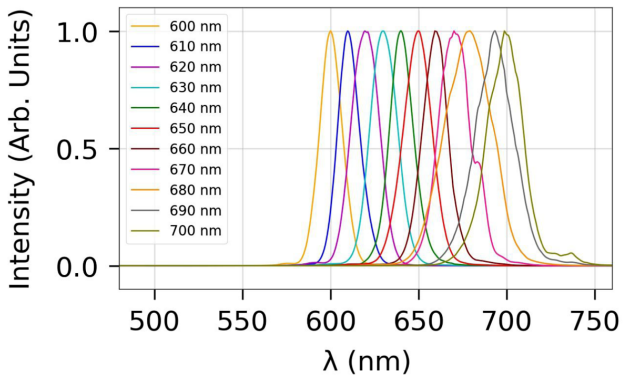

Fig. 2. Measured laser spectra used in the experiments for different central wavelengths ranging from 600 to 700 nm. All curves have been normalized to their maximum.

of about 1 mJ. After the OPA, the probe pulses are frequency-doubled using a BBO crystal, such that the tunable probe wavelength ranges from 600 to 700 nm. The pulse energy of the probe pulses has been kept constant at 270 nJ. Normalized spectra of typical pulses used in the experiments can be seen in Fig. 2. Finally, the probe beam is focused onto the sample under an angle of approximately 21°, which is the grating SPP resonance angle at a wavelength of 650 nm. The reflection of the probe pulse is measured using a Si photodiode.

Both pump and probe pulses have a duration of about 50 fs. When the pump pulse excites the sample, several types of acoustic waves are launched. These acoustic waves and their reflections change the material properties, giving rise to optical reflection changes that can be measured by the tunable, time-delayed probe pulse.

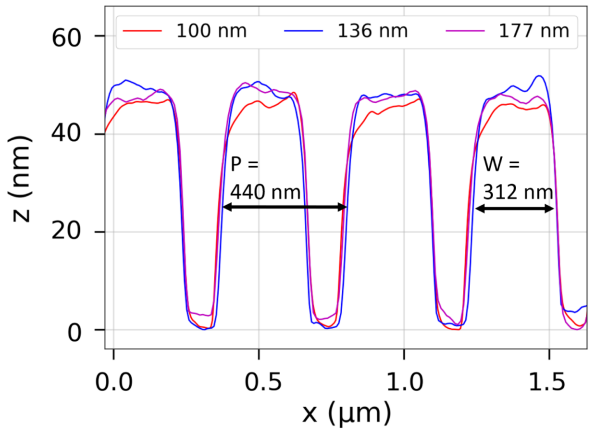

Fig. 3. AFM measurements of the grating line height profiles for Au thicknesses of 100, 136, and 177 nm. In this figure, P denotes the period of the grating, and W denotes the width of the line. The duty cycle is defined as DC = W/P.

The samples are made by thermally evaporating Au layers on top of a commercially available SiO_x grating on Si (NanoPHAB B.V.). To create the grating, 200 nm SiO_x is first fabricated on top of a Si substrate. Using electron beam lithography, a grating is defined in a photoresist on the surface of the material. After developing the resist, the grating is etched in the SiO_x using reactive-ion etching. An atomic force microscopy (AFM) image of the grating structure after Au deposition is shown in the bottom left in Fig. 1. After the deposition, the duty cycle of the grating is approximately 71%, the pitch is 440 nm, and the grating amplitude is 47 nm. The Au layer thicknesses used in our experiments are 177, 136, and 100 nm thick. In Fig. 3, we show the height profiles of the grating lines for all Au thicknesses, measured with an AFM. From this, we conclude that the grating line periodicity, amplitude, and duty cycle are comparable for all samples. We note that small differences in the shape of the grating only lead to small, static changes in the position/amplitude of the plasmonic resonance. In fact, we optimized the angle of incidence slightly for each sample to have the maximum SPP resonance at a wavelength of 650 nm. We found that changes in the angle of incidence were within our measurement accuracy of roughly half a degree.

Approximately 71% of the 400 nm pump light is absorbed by the grating structure and, for wavelengths at the SPP resonance, approximately 50% of the probe light is absorbed. In contrast, for wavelengths off-resonance, approximately 5% of the probe light is absorbed. Since the sample is optically thick, no light is transmitted.

3. RESULTS

For all measurements, both pump and probe pulse energies were kept constant at 12 μj and 270 nJ, respectively. To ensure that the probe beam experiences a homogeneous excitation profile, the focal spot diameter of the probe on the sample is 5 times smaller than that of the pump.

In Fig. 4, we plot the time-dependent pump-induced change in reflection $\Delta R/R_0$, where R_0 is the unperturbed reflection, for 11 different probe wavelengths from 600 to 700 nm on the

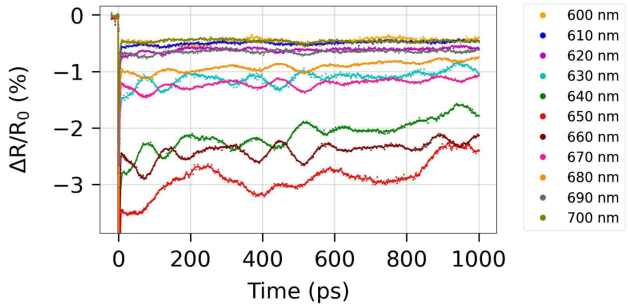

Fig. 4. Probe pulse reflection changes measured at different wavelengths as a function of time delay between the pump and probe after excitation by a 400 nm pump beam on the 177 nm thick Au layer with a 47 nm amplitude grating on top.

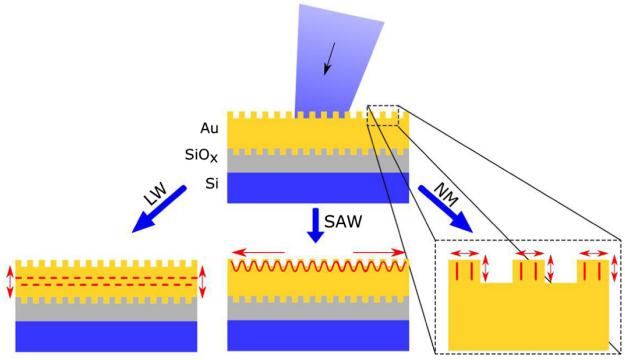

Fig. 5. Schematic depiction of the different types of acoustic excitations presumably observed in our measurements. An ultrafast laser pulse excites the plasmonic grating. The electrons absorb the light and heat up, after which they transfer their energy to the lattice, resulting in high-frequency acoustic waves. From the left to right on the bottom panel we show a schematic depiction of a LW, a SAW, and the grating line quasi-NMs. For the LW and the SAW, the red arrows indicate the direction of propagation of the acoustic waves. For the NM, the red arrows represent the direction of expansion and contraction of the grating lines. Note that the LW will partially reflect to the surface once it reaches the Au/SiO_x interface.

177 nm thick Au sample. For all probe wavelengths, we measure an instantaneous pulse-length-limited reflection decrease, governed by electron dynamics [54]. Afterward, the reflection changes show a more complex oscillatory behavior. We measure relatively low-frequency oscillations with a frequency of 2.8 GHz, most notably at a probe wavelength of 650 nm, with an amplitude of $\Delta R/R_0 \approx 1\%$. However, slightly away from the SPP resonance, in addition to a low-frequency oscillation, we also measure higher-frequency oscillations. These high-frequency oscillations are most clearly seen in the first 200 ps and are composed of at least two frequencies, namely, 6.9 and 9.1 GHz. As we will discuss later, we attribute the frequencies of 2.8, 6.9, and 9.1 GHz to a SAW, a grating line quasi-NM, and an LW, respectively. Schematic depictions of these waves are shown in Fig. 5. More frequencies appear to be present in the spectrum, which we are not yet able to identify.

A numerical fast Fourier transform (FFT) of the time-dependent measurements, after the removal of the thermal background, is shown in Fig. 6(b). The three dashed lines

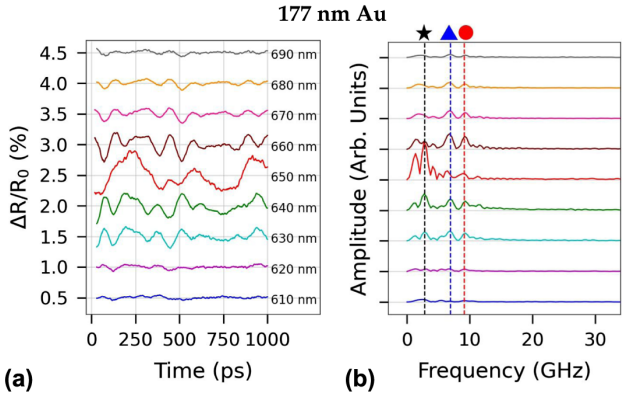

Fig. 6. (a) Probe pulse reflection changes measured at different wavelengths as a function of time delay between the pump and probe on the 177 nm thick sample, with the thermal background removed. Each curve has been given an offset for clarity; (b) FFT of the time-dependent signals. The three dashed lines, from left to right, correspond to the expected SAW, NM, and LW frequencies.

represent the three most prominent frequencies located at 2.8 (SAW), 6.9 (NM), and 9.1 GHz (LW). Below 2.8 GHz, we can see the appearance of an even lower frequency. Considering that this frequency corresponds to a period approximately equal to the entire time window of our measurement, we are reluctant to assign a real acoustic mode to it.

The amplitude and phase of the acoustic-induced reflection changes, which are extracted from the FFT, are shown versus the optical wavelength in Figs. 7(a) and 7(b), respectively. The colors of the curves correspond to the colors of the dashed lines indicated in Fig. 6(b). Figure 7(a) confirms that the optical response to the SAW is strongest when we probe the grating at the SPP resonance. With the probe wavelength on the SPP resonance, we measure an enhancement of the 2.8 GHz signal by a factor of 20 compared to measurements with the probe wavelength on the wings of the resonance. In contrast, the two higher frequencies experience a maximum on the *slope* of the SPP resonance at 640 and 660 nm probe wavelengths. These frequencies are enhanced with a factor of approximately 10 when compared to the measurements using a probe wavelength of 600 nm, but they decrease in magnitude at the SPP resonance.

In Fig. 7(b), we see that both the 6.9 GHz and the 9.1 GHz frequency components experience a phase shift of approximately π when the probe wavelength is tuned from below to above the plasmon resonance, reflecting the sign-flip seen in the time-domain data. The signal measured at 2.8 GHz shows a smaller but significant variation of the phase over the entire probe wavelength range from 610 to 700 nm.

In Figs. 8(a) and 8(c), we show the time-dependent reflection changes measured on the same sample, now with a 136 and 100 nm Au layer deposited on the grating, respectively, with the thermal background removed. Again, all wavelengths have been given a vertical offset for clarity. The FFTs of the measured signal on the 136 and 100 nm sample are shown in Figs. 8(b) and 8(d), respectively.

For the 136 nm thick Au layer, we measure transient reflection changes comparable to our 177 nm thick sample, both in shape and in size. The LW frequency, which for the sample

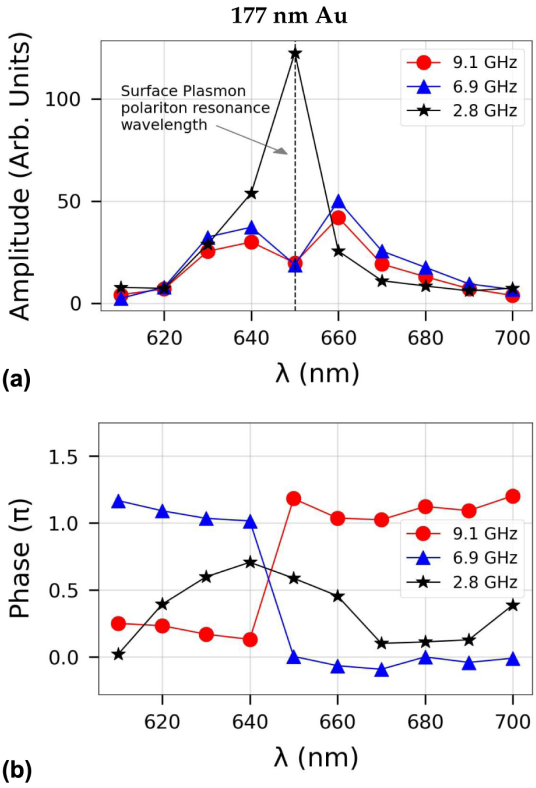

Fig. 7. (a) Amplitude of the measured reflection changes induced by the acoustic echoes extracted from the FFT of the time-domain data; (b) phase of the acoustic echoes. The Au layer has a thickness of 177 nm. The color and the symbols of the curves correspond to the frequency indicated by the vertically dashed lines with the same color and symbol as shown in Figs. 8 and 6(b).

thickness of 136 nm equals 12.0 GHz, as indicated by the rightmost dashed line in Fig. 8(b), has shifted to a higher frequency due to the decreasing thickness. The presence of another frequency around 10 GHz is also observed, but it has not been identified yet.

In contrast to the results for the 177 and 136 nm thick Au layer, for the 100 nm thick sample we measure predominantly a slowly oscillating reflection change attributed to a SAW. However, in the first 100 ps, weak higher-frequency oscillations are also observed, most clearly visible in the measurement with a probe wavelength of 630, 640, and 660 nm. These fast oscillations are attributed to the high-frequency LW. They are difficult to identify in the FFT due to their relatively low signal strength and fast decay.

In Fig. 9, we show the amplitudes and phases of the frequencies shown by the dashed lines from Figs. 8(b) and 8(c) versus the probe wavelength. The color of the curves corresponds to the color of the dashed lines. The upper two panels and the bottom two panels represent the 136 and 100 nm thick sample, respectively. For both thicknesses, we measure an enhancement of the amplitude by a factor of approximately 10 for the 2.8 GHz component when approaching the SPP from the lowest wavelength of 600 nm, and from the highest wavelength of 700 nm. For the 136 nm thick Au layer, we see that the 6.9 and the 12.0 GHz components have a weak local minimum when resonant with

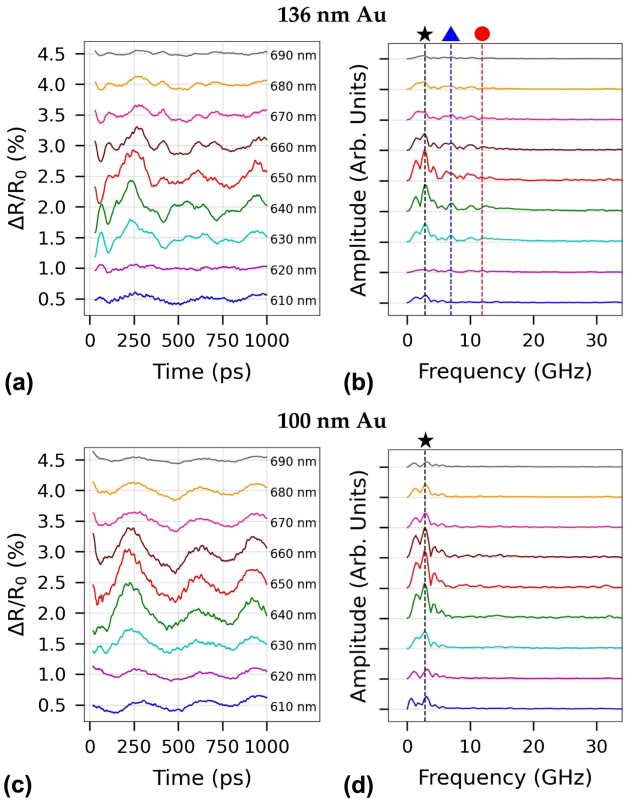

Fig. 8. (a) Reflected probe signal with the thermal background removed for the 136 nm thick Au layer and (c) for the 100 nm thick Au layer; (b) Fourier transform of the time-dependent signal for the 136 nm thick sample and (d) for the 100 nm thick sample.

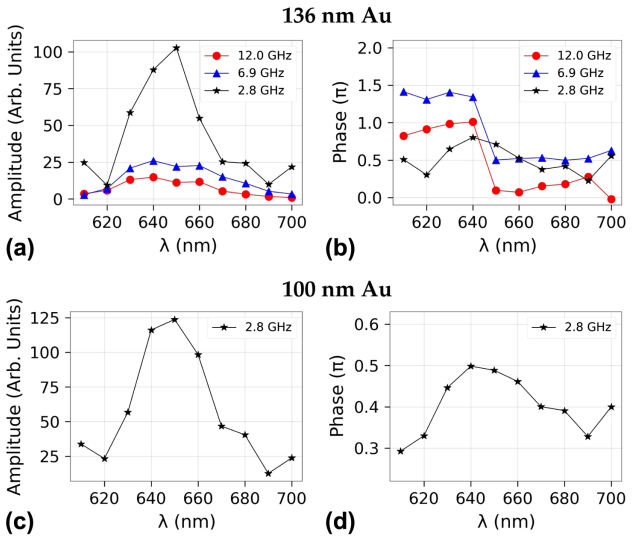

Fig. 9. (a) Amplitude of the reflection changes induced by the acoustic echoes as a function of wavelength, measured for the 136 nm thick sample and (c) for the 100 nm thick sample; (b) phase of the acoustic echoes for the 136 nm thick sample and (d) for the 100 nm thick sample. The color and the symbols of the curves correspond to the frequency indicated by the vertically dashed lines with the same color and symbol as shown in Fig. 8.

the SPP and similarly, a weak maximum in the amplitude of these frequencies on the *slopes* of the resonance.

Again, for both the 136 and 100 nm thick samples, we measure a variation in the phase for the 2.8 GHz component, around the SPP resonance. For the 6.9 (NM) and 12.0 (LW) GHz frequency components, as observed for the 136 nm sample, we measure an approximately π phase shift around the plasmon resonance, which is similar to what we see for the 177 nm thick sample. Due to the low signal strength of the LW and the NM for the 100 nm thick layer, the amplitude and phase could not be determined for these modes.

4. DISCUSSION

From our results, as discussed in the previous section, we can see that the phase and amplitude of the measured photoacoustic signals vary around the SPP resonance. Furthermore, the actual response of the amplitude and phase as a function of wavelength is different for high-frequency and low-frequency oscillations. In this section, we will first briefly attempt to identify the different types of acoustic echoes that we measure. Afterwards, we will argue that these observations may be partially explained by two effects: (1) acoustic-wave-induced changes in the free-electron density and (2) acoustic-wave-induced grating deformations.

A. Acoustic Echoes

As mentioned before, in our experiments we measure the presence of multiple acoustic frequencies. For an Au thickness of 177 nm, we measure strong peaks around 9.1, 2.8, and 6.9 GHz; see Fig. 6(b). We attribute these to LWs, SAWs, and grating line quasi-NMs, respectively, and we discuss them briefly below.

1. LW

A longitudinal acoustic wave is generated due to rapid heating of the lattice via energy transfer from the heated electron gas, causing rapid expansion of the lattice. This expansion of the lattice launches an acoustic wave that bounces back and forth between the Au/SiO_x interface and the air/Au interface, losing energy each time it reflects off the Au/SiO_x interface via partial transmission into the substrate. Near-field calculations show that most of the optical energy is deposited in the lines of the grating, but light also reaches the bottom of the valleys, in between the lines. This makes it plausible that LW waves are generated there too. As the Au has the same thickness everywhere, we expect the LWs to have the same frequency in the lines and valleys. It is possible, and even likely, that acoustic diffraction will occur near the line edges, but this is currently not taken into account.

The spatial extent of the acoustic wave is determined by the electron energy diffusion depth [27], which is about 150 nm for Au [54]. This causes the generation of two counterpropagating waves with a wavelength of approximately twice the layer thickness that form a standing wave, with a node in the middle of the layer. This leads to a periodic expansion and contraction of the whole layer. The oscillation frequency of such a wave can be found using the longitudinal speed of sound, $V_l = 3.2 \times 10^3$ m/s, and the thickness of the Au layer, d. Based on this, we calculate that the longitudinal echo should

have a frequency of $V_l/2d = 9.04$ GHz, 11.76 GHz, and 16.0 GHz for the 177, 136, and 100 nm thick sample, respectively. Considering the close proximity of the frequencies for the 177 and 136 nm sample with our measured frequencies of 9.1 and 12.0 GHz, we attribute these frequencies to a longitudinal standing wave. For the 100 nm sample thick sample, the LW frequency equals $f_{lw} = 16.0$ GHz. However, due to the low amplitude of this oscillation in comparison to the SAW and due to the apparent higher damping rate, this frequency is not clearly visible in the FFT shown in Fig. 8(d).

In the 177 nm and the 136 nm thick sample, we measure a dip in the amplitude of the reflection change induced by the longitudinal echo when the probe is tuned to the SPP resonance, as can be seen in Figs. 7(a) and 9(a). We also measure an increase in the reflection change from the longitudinal echo for both thicknesses on the slopes of the resonance at a wavelength corresponding to 640 and 660 nm.

2. SAW

A SAW is an acoustic wave that travels along the surface of the material. A SAW can be excited if there is a spatial inhomogeneity in either the excitation profile [3,55–57] or in the surface topography [51]. However, such a wave is not necessarily confined to the surface. The type of SAW potentially present in our experiment are a Rayleigh wave, a Lamb wave, or a shear wave.

A Rayleigh wave has a finite penetration depth into the metal [50,52]. For a bulk Au layer, we can calculate that relative vertical displacement of such a wave reaches a value of $1/e$ at a depth of 275 nm [58], which exceeds all layer thicknesses reported in this paper. This indicates that it is unlikely that our measured SAW is a pure Rayleigh wave.

A Lamb wave is, generally speaking, a wave that is confined by two free surfaces and can be viewed as a guided mode [59]. Since our Au layer is not confined by two free surfaces but rather an Au/SiO_x and Au/air interface, the presence of a Lamb wave seems unlikely. A shear wave is a wave that travels through the entire bulk with a k-vector parallel to the surface, similar to a Rayleigh and Lamb wave [58].

A shear wave displaces the lattice orthogonal to its k-vector. By definition, it is a property of a shear wave that it does not alter the density of the material [58]. This would seem to be in agreement with the fact that the SAW signal does not peak at the slopes of the SPP resonance, which would be the case if it were sensitive to density changes, as we will explain below. The velocity of a shear wave equals the transverse sound velocity [58], which for Au equals approximately 1200 m/s [60]. When a periodic structure is present on a surface, the periodicity of the surface structure determines the wavelength of the dominant surface wave [22,49], which in our experiments equals 440 nm. Taking the velocity and the periodicity into account, the predicted frequency of the SAW equals $f_{SAW} = 2.7$ GHz. Considering the close proximity of the calculated frequency to the 2.8 GHz signal observed for all our measured thicknesses, the excited and measured SAW is most likely a shear wave.

3. Grating Line Quasi-NM

A grating line NM is the expansion and contraction of individual isolated metallic bars. Here, considering that the lines are attached to an Au layer, we think it is more appropriate to speak of quasi-NMs. Under similar experimental conditions, the grating line quasi-NM for one-dimensional Au rectangular bars with a 50% duty cycle, a thickness of 40 nm, and a pitch of 400 nm on a quartz substrate has been measured at 7.78 GHz [52] by Lin *et al*. If we extrapolate from their data to a grating amplitude of 50 nm, we find a NM frequency of 7.1 GHz, which is close to our measured frequency of 6.9 GHz. Discrepancies between our measured frequency and the calculated frequency from Lin *et al.* are probably caused by the fact that we have an Au substrate for our Au bars, instead of quartz. Furthermore, our periodicity and duty cycle are slightly different from those of Lin *et al*. The effect of this is difficult to predict precisely. Nevertheless, it seems plausible to attribute the 6.9 GHz frequency to the grating line quasi-NM.

B. Acoustically Induced SPP Resonance Frequency Variations

In this section, we will describe two possible ways by which the SPP resonance frequency can shift due to the presence of acoustic waves. They are acoustically induced electron density changes, and acoustic-wave-induced grating deformation. A strongly exaggerated schematic depiction of this process of shifting the SPP resonance is shown in Fig. 10. The acoustic echoes can both decrease and increase the SPP resonance frequency, as we will explain below. Therefore, the SPP resonance will periodically oscillate around the unperturbed resonance wavelength. Note that the presence of an acoustic wave might also possibly influence the interband transitions of our sample [20,21], altering the dielectric function across the entire spectrum. We are currently unable to calculate the effect of the density changes on the frequency and strength of the interband transitions.

1. Acoustical-Wave-Induced Electron Density Changes

In our setup, the acoustic-wave-induced electron density changes cannot directly be measured. However, to test the hypothesis that the change of the free-electron density can give rise to the optical response that we observe, we can calculate the

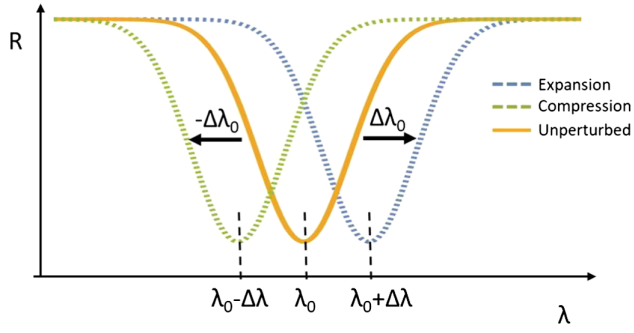

Fig. 10. Schematic representation of the acoustically induced change in the SPP resonance; compression due to the acoustic echo causes the SPP resonance wavelength to decrease while expansion causes the SPP resonance wavelength to increase.

shift of the plasmonic resonance wavelength as a function of the electron density. The main principle behind this hypothesis is that many types of acoustic waves consist of propagating regions of higher and lower material density. The electron density will semi-instantaneously follow the acoustic-wave-induced lattice density changes to maintain charge neutrality [61]. Changes in the free-electron density will in turn change the plasma frequency $\omega_p = \sqrt{N_e e^2/\epsilon_0 m}$, where N_e is the free-electron density, e the electronic charge, ϵ_0 the vacuum permittivity of space, and m the effective electron mass. Changes in the plasma frequency cause changes in the dielectric constant and, thus, the position of the SPP resonance.

To successfully excite a surface plasmon, the sum of the scalar value of the x component of the probe wave vector and the grating wavenumber must be equal to the plasmonic wavenumber [62]. The SPP excitation condition then is

$$\left|\frac{\lambda_0}{2\pi}\sin\theta \pm N\frac{2\pi}{\Lambda}\right| = k_{\mathrm{SPP}} = \frac{\lambda_0}{2\pi}\sqrt{\frac{\epsilon_m\epsilon_d}{\epsilon_m+\epsilon_d}}, \qquad (1)$$

where λ_0 is the vacuum wavelength of the light, θ the angle of incidence with respect to the surface normal, N the plasmonic order which, under our experimental conditions, is 1, Λ the grating pitch, k_{SPP} the SPP wavenumber, and ϵ_m and ϵ_d the frequency-dependent dielectric functions of the metal (Au) and the dielectric (air), respectively. For convenience, we will assume that the imaginary parts of the dielectric functions are small compared to their real parts and can, therefore, be neglected. The dielectric constant of air, ε_d, is taken as 1. For a given Λ and θ, Eq. (1) allows us to determine the SPP resonance wavelength. Furthermore, from Eq. (1) it is clear that the SPP resonance wavelength is dependent on the dielectric function of the material. If the dielectric function of the metal would change due to an external perturbation, such as an acoustic wave, the plasmon resonance wavelength will shift [35,41,42,47,63].

Looking at Fig. 6(b), as discussed before, we measure multiple acoustic frequencies. The frequencies of 2.8, 6.9, and 9.1 GHz have been tentatively identified as a surface wave, a grating line quasi-NM, and a LW, respectively. When the SPP resonance oscillates due to the presence of an electron density perturbation, this should result in a π-phase shift of the reflection change when the reflection is measured above compared to below the SPP resonance, as can be seen in Fig. 10. When we look at the phase of the reflection changes, as shown in Fig. 7(b), we see that such a phase shift is only present for the 6.9 and 9.1 GHz frequencies and *not* for the 2.8 GHz frequency. This could indicate that the LW and NM mode both induce electron density changes, resulting in oscillations of the SPP, whereas the SAW does not induce electron density changes. This is consistent with the assumption that the 2.8 GHz wave is indeed a shear wave, since a shear wave does not induce density changes.

In the presence of the longitudinal and quasi-normal acoustic modes, the lattice density will change depending on the displacement of the atoms. Using an advanced 2D numerical model [3] that incorporates the generation and propagation of acoustic waves in single *flat* Au layers, we are able to calculate that the expansion and contraction under our experimental conditions equals approximately ± 150 pm. It is not unreasonable to assume that similar expansion and contraction amplitudes are present in our grating structure. This expansion and contraction results in electron density oscillations with maximum values between $0.999 \times N_{e,0}$ and $1.001 \times N_{e,0}$, where $N_{e,0}$ is the unperturbed electron density. These oscillations in electron density result in a change of the dielectric function through the plasma frequency, which would be probed in a volume determined by the penetration depth of the probe light in our experiment. If we use this acoustically altered dielectric function in Eq. (1), we find that the maximum plasmon resonance wavelength shift, $\Delta\lambda_{0,\max}$, equals 0.05 nm. Although such a shift seems small, we calculate that it results in a reflection change of approximately $\pm 0.2\%$ at a wavelength of 640 nm. If we look at Fig. 4, we see that this is close to the amplitude of our measured oscillatory reflection changes. A similar argument holds for reflection changes measured for different probe wavelengths.

2. Acoustic-Wave-Induced Grating Deformations

In addition to electron density variations, acoustic waves also alter the grating structure. Displacement of the atoms by the acoustic waves results in a change of the grating amplitude and the duty cycle, both of which are known to influence the SPP resonance and, thus, the wavelength-dependent reflection [64]. Numerical simulations were performed to see the effect of grating amplitude changes and duty-cycle changes on the SPP resonance. The numerical calculations were performed using "Cyclops," an in-house-developed program that solves Maxwell's equations [65]. It is based on the finite-element method described by Lalanne *et al*. [66] and was tested and benchmarked against other methods such as the finite-difference time-domain method.

To calculate the shift of the SPP resonance as a function of grating depth and duty cycle, 2D simulations were performed for optical wavelengths ranging from 300 to 800 nm for different grating amplitudes. In Fig. 11, we plot the SPP resonance wavelength as a function of grating amplitude. We note that around our grating amplitude of 47 nm, the dependence of the SPP resonance on the grating amplitude is almost linear. From these calculations, we extract that the $\Delta\lambda_{\mathrm{SPP}}/\Delta A = 2.25$, where ΔA is the change in grating amplitude. For the duty cycle, we can look at how much the SPP resonance shifts as a function of the valley width. A similar analysis, as with the grating amplitude, shows that $\Delta\lambda_{\mathrm{SPP}}/\Delta d_v = 0.25$, where d_v is the width of the valley of the grating. From this we conclude that relative grating amplitude variations shift the SPP resonance more than relative duty-cycle variations. The amplitude of the grating can only change when there is a difference in acoustic-wave-induced vertical expansion/contraction in the valleys and the ridges of the grating. We cannot assume *a priori* that the ridges and valleys expand and contract with the same phase and amplitude. Such differences in the grating amplitude can, in fact, arise due to differences in absorption of the pump light in the ridges and valleys of the grating. The calculated spatial distribution of the light absorption, as shown in Fig. 12, demonstrates that there is indeed a difference in the amount of absorbed light in the valleys and ridges of the grating. In Au, electron energy diffusion is rapid but does not *fully* homogenize the temperatures in our grating structure. Therefore, we expect that different lattice temperature changes in the ridges and the valleys of the

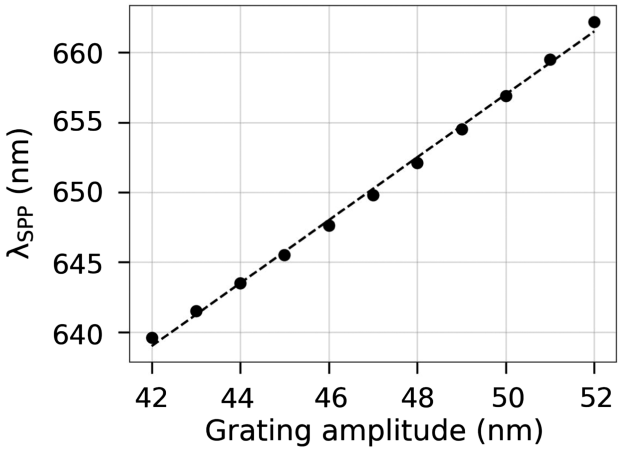

Fig. 11. SPP resonance wavelength λ_{SPP} as a function of the grating amplitude for an Au thickness of 177 nm, computed via simulation. The dashed curve represents a linear fit to the data.

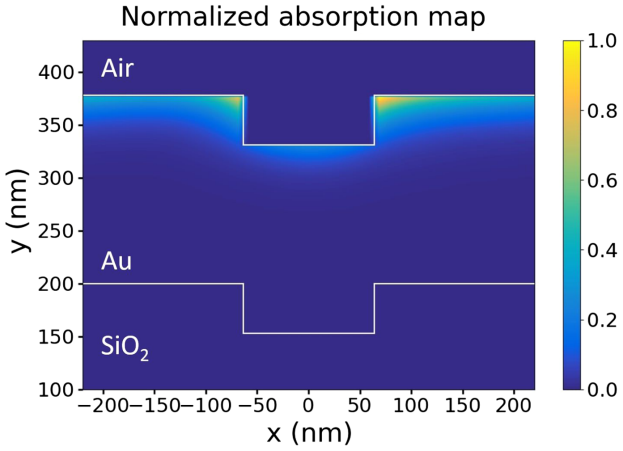

Fig. 12. Simulated normalized absorption of the 400 nm pump beam. We find that the absorption is mostly localized on the ridges of the grating. For clarity, the absorption in air is not shown.

grating are likely. We can thus expect acoustically induced vertical expansion differences between the ridges and the valleys of the grating. We calculate that in order to induce reflection changes with a similar magnitude as seen in our measurements, the grating amplitude would have to change with a maximum amplitude of only ±35 pm, which is plausible.

Both the electron density variation and changes in the grating amplitude are suitable candidates to explain our measured results. We cannot currently exclude either model as an explanation for the effects we observe when probing around the SPP resonance.

5. CONCLUSION

We have studied the generation and detection of acoustic waves on a plasmonic grating. We have shown time-dependent reflection changes caused by acoustic echoes of which the detection was enhanced at probe wavelengths around the SPP resonance. We demonstrate the simultaneous presence of multiple acoustic waves, of which the most prominent are the longitudinal, quasi-normal and SAW modes. Our measurements show an enhancement of the longitudinal and the quasi-NM-induced reflection changes by a factor of 10 on the slopes of the resonance and an enhancement of the SAW mode on the peak of the resonance by a factor of 20, compared to the measurements with a probe wavelength on the wings of the resonance.

Using a simple model that calculates the shift of the SPP resonance as a function of electron density, we are able to reproduce the magnitude and the phase of the reflection changes for the longitudinal and NMs. Besides the presence of electron density variations, we also argue that acoustic-wave-induced grating deformations may play a significant role in the measured reflection changes. Both proposed mechanisms are capable of explaining our measured results. There is no *a priori* reason to assume that these two effects do not both influence the measured reflection change simultaneously, although our results do not currently allow us to determine which one dominates.

Funding. ASML; Nederlandse Organisatie voor Wetenschappelijk Onderzoek; Universiteit van Amsterdam.

Acknowledgment. The authors would like to thank Dr. Rudolf Sprik (University of Amsterdam) for discussions about and simulations of SAWs.

Disclosures. The authors declare no conflict of interest.

Data Availability. Data underlying the results presented in this paper are not publicly available at this time but may be obtained from the authors upon reasonable request.

[†]These authors contributed equally to this paper.

REFERENCES

1. C. Thomsen, H. T. Grahn, H. J. Maris, and J. Tauc, "Surface generation and detection of phonons by picosecond light pulses," Phys. Rev. B **34**, 4129–4138 (1986).
2. O. Matsuda, M. C. Larciprete, R. Li Voti, and O. B. Wright, "Fundamentals of picosecond laser ultrasonics," Ultrasonics **56**, 3–20 (2015).
3. H. Zhang, A. Antoncecchi, S. Edward, I. Setija, P. Planken, and S. Witte, "Unravelling phononic, opto-acoustic and mechanical properties of metals with light-driven hypersound," Phys. Rev. Appl. **10**, 014010 (2020).
4. P. Ruello and V. E. Gusev, "Physical mechanisms of coherent acoustic phonons generation by ultrafast laser action," Ultrasonics **56**, 21–35 (2015).
5. P. van Capel, *Ultrafast Nonlinear Acoustics in Crystals and Nanostructures* (University of Utrecht, 2008).
6. M. V. Exter and A. Lagendijk, "Ultrashort surface-plasmon and phonon dynamics," Phys. Rev. Lett. **60**, 49–52 (1988).
7. T. Saito, O. Matsuda, and O. B. Wright, "Picosecond acoustic phonon pulse generation in nickel and chromium," Phys. Rev. B **67**, 205421 (2003).
8. J. L. Arlein, S. E. Palaich, B. C. Daly, P. Subramonium, and G. A. Antonelli, "Optical pump-probe measurements of sound velocity and thermal conductivity of hydrogenated amorphous carbon films," J. Appl. Phys. **104**, 033508 (2008).
9. G. Tas and H. J. Maris, "Electron diffusion in metals studied by picosecond ultrasonics," Phys. Rev. B **49**, 15046–15054 (1994).
10. V. E. Gusev and O. B. Wright, "Ultrafast nonequilibrium dynamics of electrons in metals," Phys. Rev. B **57**, 2878–2888 (1998).
11. O. B. Wright and V. E. Gusev, "Acoustic generation in crystalline silicon with femtosecond optical pulses," Appl. Phys. Lett. **66**, 1190–1192 (1995).
12. V. E. Gusev, "On the duration of acoustic pulses excited by subpicosecond laser action on metals," Opt. Commun. **94**, 76–78 (1992).

13. J. Wang and C. Guo, "Effect of electron heating on femtosecond laser-induced coherent acoustic phonons in noble metals," Phys. Rev. B **75**, 184304 (2007).
14. O. B. Wright and K. Kawashima, "Coherent phonon detection from ultrafast surface vibrations," Phys. Rev. Lett. **69**, 1668–1671 (1992).
15. A. Devos and C. Lerouge, "Evidence of laser-wavelength effect in picosecond ultrasonics: Possible connection with interband transitions," Phys. Rev. Lett. **86**, 2669–2672 (2001).
16. A. Devos, R. Cote, G. Caruyer, and A. Lefvre, "A different way of performing picosecond ultrasonic measurements in thin transparent films based on laser-wavelength effects," Appl. Phys. Lett. **86**, 211903 (2005).
17. D. Schneider, T. Witke, T. Schwarz, B. Schoneich, and B. Schultrich, "Testing ultra-thin films by laser-acoustics," Surf. Coatings Technol. **126**, 136–141 (2000).
18. H. T. Grahn, H. J. Maris, and J. Tauc, "Time-resolved study of vibrations of a-Ge:H/a-Si:H multilayers," Phys. Rev. B **38**, 6066–6074 (1988).
19. B. Perrin, B. Bonello, J. C. Jeannet, and E. Romatet, "Picosecond ultrasonics study of metallic multilayers," Physica B **219–220**, 681–683 (1996).
20. A. Devos and A. Le Louarn, "Strong effect of interband transitions in the picosecond ultrasonics response of metallic thin films," Phys. Rev. B **68**, 045405 (2003).
21. A. Devos and R. Cote, "Strong oscillations detected by picosecond ultrasonics in silicon: evidence for an electronic-structure effect," Phys. Rev. B **70**, 125208 (2004).
22. R. I. Tobey, E. H. Gershgoren, M. E. Siemens, M. M. Murnane, H. C. Kapteyn, T. Feurer, and K. A. Nelson, "Nanoscale photothermal and photoacoustic transients probed with extreme ultraviolet radiation," Appl. Phys. Lett. **85**, 564–566 (2004).
23. R. I. Tobey, M. E. Siemens, M. M. Murnane, H. C. Kapteyn, D. H. Torchinsky, and K. A. Nelson, "Transient grating measurement of surface acoustic waves in thin metal films with extreme ultraviolet radiation," Appl. Phys. Lett. **89**, 091108 (2006).
24. G. A. Antonelli, P. Zannitto, and H. J. Maris, "New method for the generation of surface acoustic waves of high frequency," Physica B **316–317**, 377–379 (2002).
25. T. Saito, O. Matsuda, M. Tomoda, and O. B. Wright, "Imaging gigahertz surface acoustic waves through the photoelastic effect," J. Opt. Soc. Am. B **27**, 2632–2638 (2010).
26. M. R. Armstrong, E. J. Reed, K. Y. Kim, J. H. Glownia, W. M. Howard, E. L. Piner, and J. C. Roberts, "Observation of terahertz radiation coherently generated by acoustic waves," Nat. Phys. **5**, 285–288 (2009).
27. S. Edward, H. Zhang, I. Setija, V. Verrina, A. Antoncecchi, S. Witte, and P. C. M. Planken, "Detection of hidden gratings through multilayer nanostructures using light and sound," Phys. Rev. Appl. **10**, 014015 (2019).
28. V. Verrina, S. Edward, H. Zhang, S. Witte, and P. C. M. Planken, "Photoacoustic detection of low duty cycle gratings through optically opaque layers," Appl. Phys. Lett. **117**, 051104 (2020).
29. T. F. Crimmins, A. A. Maznev, and K. A. Nelson, "Transient grating measurements of picosecond acoustic pulses in metal films," Appl. Phys. Lett. **74**, 1344–1346 (1999).
30. R. W. Wood, "On a remarkable case of uneven distribution of light in a diffraction grating spectrum," Philos. Mag. **4**(21), 396–402 (1902).
31. H. P. Chen, Y. C. Wen, Y. H. Chen, C. H. Tsai, K. L. Lee, P. K. Wei, J. K. Sheu, and C. K. Sun, "Femtosecond laser-ultrasonic investigation of plasmonic fields on the metal/gallium nitride interface," Appl. Phys. Lett. **97**, 201102 (2010).
32. R. Nuster, G. Paltauf, and P. Burgholzer, "Comparison of surface plasmon resonance devices for acoustic wave detection in liquid," Opt. Express **15**, 6087–6095 (2007).
33. K. Katayama, T. Sawada, and Q. Shen, "Detection of photoinduced electronic, thermal, and acoustic dynamics of gold film using a transient reflecting grating method under three types of surface plasmon resonance conditions," Phys. Rev. B **58**, 8428–8436 (1998).
34. E. Kretschmann, "Die Bestimmung optischer Konstanten von Metallen durch Anregung von Oberflächenplasmaschwingungen," Z. Phys. **241**, 313–324 (1971).
35. J. Wang, J. Wu, and C. Guo, "Resolving dynamics of acoustic phonons by surface plasmons," Opt. Lett. **32**, 719–721 (2007).
36. N. Rotenberg, J. N. Caspers, and H. M. Van Driel, "Tunable ultrafast control of plasmonic coupling to gold films," Phys. Rev. B **80**, 245420 (2009).
37. R. H. Ritchie, E. T. Arakawa, J. J. Cowan, and R. N. Hamm, "Surface-plasmon resonance effect in grating diffraction," Phys. Rev. Lett. **21**, 1530–1533 (1968).
38. H. Raether, *Surface Plasmons on Smooth and Rough Surfaces and on Gratings*, Vol. **111** of Springer Tracts in Modern Physics (Springer-Verlag, 1988).
39. L. E. Kreilkamp, I. A. Akimov, V. I. Belotelov, B. A. Glavin, L. V. Litvin, A. Rudzinski, M. Kahl, R. Jede, M. Wiater, T. Wojtowicz, G. Karczewski, D. R. Yakovlev, and M. Bayer, "Terahertz dynamics of lattice vibrations in Au/CdTe plasmonic crystals: photoinduced segregation of Te and enhancement of optical response," Phys. Rev. B **93**, 125404 (2016).
40. N. Khokhlov, G. Knyazev, B. Glavin, Y. Shtykov, O. Romanov, and V. Belotelov, "Interaction of surface plasmon polaritons and acoustic waves inside an acoustic cavity," Opt. Lett. **42**, 3558–3561 (2017).
41. V. V. Temnov, "Ultrafast acousto-magneto-plasmonics," Nat. Photonics **6**, 728–736 (2012).
42. V. V. Temnov, C. Klieber, K. A. Nelson, T. Thomay, V. Knittel, A. Leitenstorfer, D. Makarov, M. Albrecht, and R. Bratschitsch, "Femtosecond nonlinear ultrasonics in gold probed with ultrashort surface plasmons," Nat. Commun. **4**, 3–8 (2013).
43. J. H. Hodak, I. Martini, and G. V. Hartland, "Observation of acoustic quantum beats in nanometer sized Au particles," J. Chem. Phys. **108**, 9210–9213 (1998).
44. J. H. Hodak, A. Henglein, and G. V. Hartland, "Size dependent properties of Au particles: coherent excitation and dephasing of acoustic vibrational modes," J. Chem. Phys. **111**, 8613–8621 (1999).
45. G. V. Hartland, "Coherent vibrational motion in metal particles: determination of the vibrational amplitude and excitation mechanism," J. Chem. Phys. **116**, 8048–8055 (2002).
46. G. V. Hartland, "Coherent excitation of vibrational modes in metallic nanoparticles," Annu. Rev. Phys. Chem. **57**, 403–430 (2006).
47. Z. Chen and M. F. Decamp, "Measuring optical phonon dynamics in a bismuth thin film through a surface plasmon resonance," J. Appl. Phys. **112**, 013527 (2012).
48. D. H. Hurley and K. L. Telschow, "Picosecond surface acoustic waves using a suboptical wavelength absorption grating," Phys. Rev. B **66**, 153301 (2002).
49. D. H. Hurley, R. Lewis, O. B. Wright, and O. Matsuda, "Coherent control of gigahertz surface acoustic and bulk phonons using ultrafast optical pulses," Appl. Phys. Lett. **93**, 113101 (2008).
50. B. Bonello, A. Ajinou, V. Richard, P. Djemia, and S. M. Chérif, "Surface acoustic waves in the GHz range generated by periodically patterned metallic stripes illuminated by an ultrashort laser pulse," J. Acoust. Soc. Am. **110**, 1943–1949 (2001).
51. Q. Li, K. Hoogeboom-Pot, D. Nardi, M. M. Murnane, H. C. Kapteyn, M. E. Siemens, E. H. Anderson, O. Hellwig, E. Dobisz, B. Gurney, R. Yang, and K. A. Nelson, "Generation and control of ultrashort-wavelength two-dimensional surface acoustic waves at nanoscale interfaces," Phys. Rev. B **85**, 195431 (2012).
52. H. N. Lin, H. J. Maris, L. B. Freund, K. Y. Lee, H. Luhn, and D. P. Kern, "Study of vibrational modes of gold nanostructures by picosecond ultrasonics," J. Appl. Phys. **73**, 37–45 (1993).
53. M. Colletta, W. Gachuhi, S. A. Gartenstein, M. M. James, E. A. Szwed, B. C. Daly, W. Cui, and G. A. Antonelli, "Picosecond ultrasonic study of surface acoustic waves on periodically patterned layered nanostructures," Ultrasonics **87**, 126–132 (2018).
54. S. Edward, A. Antoncecchi, H. Zhang, H. Sielcken, S. Witte, and P. C. M. Planken, "Detection of periodic structures through opaque metal layers by optical measurements of ultrafast electron dynamics," Opt. Express **26**, 23380–23396 (2018).
55. Z. H. Shen, B. Q. Xu, X. W. Ni, J. Lu, and S. Y. Zhang, "Theoretical study on line source laser-induced surface acoustic waves in two-layer structure in ablative regime," Opt. Laser Technol. **36**, 139–143 (2004).

56. A. M. Aindow, R. J. Dewhurst, and S. B. Palmer, "Laser-generation of directional surface acoustic wave pulses in metals," Opt. Commun. **42**, 116–120 (1982).
57. A. Harata, H. Nishimura, and T. Sawada, "Laser-induced surface acoustic waves and photothermal surface gratings generated by crossing two pulsed laser beams," Appl. Phys. Lett. **57**, 132–134 (1990).
58. J. L. Rose, *Ultrasonic Guided Waves in Solid Media* (Cambridge University Press, 2014).
59. H. Zhang, A. Antoncecchi, S. Edward, P. Planken, and S. Witte, "Ultrafast laser-induced guided elastic waves in a freestanding aluminum membrane," Phys. Rev. B **103**, 064303 (2021).
60. R. D. Lide, "CRC handbook of chemistry and physics," J. Am. Chem. Soc. **126**, 1586 (2004).
61. D. J. Griffiths, *Introduction to Electrodynamics*, 3rd ed. (Prentice Hall, 1999).
62. G. K. Ramanandan, G. Ramakrishnan, N. Kumar, A. J. Adam, and P. C. M. Planken, "Emission of terahertz pulses from nanostructured metal surfaces," J. Phys. D **47**, 374003 (2014).
63. A. Derkachova, K. Kolwas, and I. Demchenko, "Dielectric function for gold in plasmonics applications: size dependence of plasmon resonance frequencies and damping rates for nanospheres," Plasmonics **11**, 941–951 (2016).
64. Y. C. Chang, P. Zhou, and J. H. Burge, "Analysis of phase sensitivity for binary computer-generated holograms," Appl. Opt. **45**, 4223–4234 (2006).
65. X. Wei, A. J. Wachters, and H. P. Urbach, "Finite-element model for three-dimensional optical scattering problems," J. Opt. Soc. Am. A **24**, 866–881 (2007).
66. M. Besbes, J. P. Hugonin, P. Lalanne, S. van Haver, O. T. Janssen, A. M. Nugrowati, M. Xu, S. F. Pereira, H. P. Urbach, A. S. van de Nes, P. Bienstman, G. Granet, A. Moreau, S. Helfert, M. Sukharev, T. Seideman, F. I. Baida, B. Guizal, and D. Van Labeke, "Numerical analysis of a slit-groove diffraction problem," J. Eur. Opt. Soc. **2**, 07022 (2007).